Journal of Catalysis 258 (2008) 177–186

Contents lists available at ScienceDirect

Journal of Catalysis

www.elsevier.com/locate/jcat

Modification of CeO_2–ZrO_2 mixed oxides by coprecipitated/impregnated Sr: Effect on the microstructure and oxygen storage capacity

Jun Fan, Duan Weng *, Xiaodong Wu, Xiaodi Wu, Rui Ran

Laboratory of Advanced Materials, Department of Materials Science and Engineering, Tsinghua University, Beijing 100084, China

ARTICLE INFO

Article history:
Received 14 April 2008
Revised 5 June 2008
Accepted 5 June 2008
Available online 11 July 2008

Keywords:
CeO_2–ZrO_2 mixed oxides
Strontium
Impregnation
OSC
Interface

ABSTRACT

Strontium was introduced to modify CeO_2–ZrO_2 mixed oxides (CZ) by two methods, coprecipitation (CZS) and impregnation (SCZ). Structural and textural characterizations revealed that Sr could retard the sintering of oxide particles and restrict the phase segregation during the hydrothermal ageing treatment. Specifically, the impregnation method brought about a more satisfying thermal stability of the modified CZ. This phenomenon was attributed to the enrichment of Sr on the particle surface and the formation of $SrZrO_3$ phase. The reducibility of the oxides was investigated by means of the oxygen storage capacity (OSC), and aged SCZ (SCZa) presented the best OSC performance. The reduction-ratio-dependent activation energy (E_a) was extremely low for the surface reduction of SCZa, suggesting the participation of highly active oxygen. The $SrZrO_3$/CeO_2–ZrO_2 interface was considered as the possible origin of this oxygen species. During bulk reduction, the effect of Sr on enhancing the reducibility was evident as well.

1. Introduction

CeO_2–ZrO_2 mixed oxides (CZ) have been considered as an outstanding oxygen storage material (OSM) in three-way catalysts (TWCs), which aim at the simultaneous purification of CO, HC and NO_x in automotive exhaust [1–4]. To evaluate oxygen storage capacity (OSC), a lot of parameters, such as dynamic oxygen storage capacity (DOSC) [5], oxygen storage capacity complete (OSCC) [6], oxygen transport capacity (OTC) [7] and oxygen buffering capacity (OBC) [8], have been defined to score the oxygen storage/release capacity of ceria and ceria-based oxides. Up to now, many studies have been directed to explore the effects of composition [9–11], phase structure [12–14] and atomic arrangement in crystal lattice [15,16] on the OSC properties of CZ. In general, the key role of oxygen vacancies in enhancing oxygen mobility is acknowledged by many research groups.

As more and more rigorous emission regulations is being applied, ceria-based materials with better OSC performance and higher thermal stability are required for the further development of durable, highly active and versatile TWCs. The rare earth elements are one group of the most common dopants to improve the OSC and thermal stability of ceria and ceria-based oxides. Lanthanum [17] and yttrium [18] are among the early additives for the modification of ceria. In recent studies, our group [19] found that the doping of Pr and Nd led to a lattice deformation of tetragonal CZ to a pseudocubic structure. Compared with CZ, the doped samples presented higher ratio of Ce^{3+}/Ce^{4+}, created more crystal defects, and maintained relatively higher surface area after hydrothermal ageing. The doping effects of alkaline earth metal on the OSC properties and thermal stability of CZ have been also widely investigated. It was reported that CaO could create strain in the fluorite-type CeO_2–ZrO_2 lattice and strongly modify the surface and bulk oxygen handling properties [20]. Inaba and Tagawa [21] reported that Sr^{2+} and Ca^{2+} had the optimum ionic radii and gave the minimum association enthalpy between dopant ions and oxygen vacancies, which implied improved oxygen mobility in ceria-based materials. In the research by An et al. [22], the deteriorated OSC of MgO doped $Ce_{0.67}Zr_{0.33}O_2$ after redox treatment was attributed to the small solubility of Mg^{2+} in ceria lattice and the collapse of defective structure of Mg–Ce–Zr–O system.

In this work, strontium was introduced to modify CZ not only by doping but also by impregnation method. The microstructural and textural properties of fresh and hydrothermally aged samples were compared to exhibit the effect of Sr on the thermal stability of CZ. The OSC performances of aged samples were evaluated under both transient and static conditions, using CO oxidation as probe reaction. The relationship between the distribution of Sr^{2+} in/on CZ particles and the physical/chemical properties of ceria–zirconia mixed oxides was constructed.

* Corresponding author. Fax: +86 10 62772726.
E-mail address: duanweng@tsinghua.edu.cn (D. Weng).

0021-9517/$ – see front matter
doi:10.1016/j.jcat.2008.06.009

2. Experimental

2.1. Catalyst preparation

Fresh CeO_2–ZrO_2 mixed oxides (CZf) were obtained by oxidative coprecipitation method. The nitrates $Ce(NO_3)_3{\cdot}6H_2O$ and $ZrO(NO_3)_2{\cdot}5H_2O$ served as precursors. The mixture of hydrogen peroxide solution (30 wt%), ammonia water (25 wt%) and deionized water according to the volume ratio of 1:4:4 was applied as precipitator. The precipitate was formed at room temperature and a stirring speed of ca. 1200 rpm was required during the precipitation procedure. After being dried at 110 °C for 12 h, the precipitate was submitted to decomposition at 300 °C for 1 h and calcination at 700 °C for 3 h. The nominal composition of the mixed oxides could be denoted as $Ce_{0.67}Zr_{0.33}O_2$.

To obtain fresh Sr-doped CeO_2–ZrO_2 mixed oxides (CZSf), the nitrates $Ce(NO_3)_3{\cdot}6H_2O$, $Zr(NO_3)_4{\cdot}5H_2O$ and $Sr(NO_3)_2$ were mixed as precursors. The atomic ratio of Ce:Zr was also 67:33, and the theoretical mass percentage of SrO in the oxides was 3%. The successive process followed the oxidative coprecipitation process for CZf.

Another type of fresh Sr-loaded CeO_2–ZrO_2 mixed oxides (SCZf) were obtained by impregnation method. The as-prepared CZf powders were impregnated in the aqueous solution of $Sr(NO_3)_2$ and subsequently calcined at 700 °C for 1 h for the decomposition of $Sr(NO_3)_2$. The nominal weight content of SrO in SCZf was 3% as well.

These as-prepared fresh samples, denoted as CZf, CZSf and SCZf, were further submitted to hydrothermal ageing at 1050 °C for 5 h in 7% steam/air. The obtained aged powders were then denoted as CZa, CZSa and SCZa.

2.2. Characterizations

The X-ray diffraction (XRD) analysis was conducted on a Japan Science D/max-RB diffractometer employing Cu$K\alpha$ radiation ($\lambda = 1.5418$ Å). The X-ray tube was operated at 45 kV and 150 mA. The X-ray powder diffractograms were recorded at 0.02° intervals in the range $20° \leqslant 2\theta \leqslant 80°$ with 2 s count accumulation per step. The crystal phase was identified with the help of the JCPDS cards. The calculations and analyses based on the XRD data were assisted by the THX application software and the peak fitting was acquired according to a pseudo-Voigt profile function. The lattice parameters were calculated with the application of least-squares refinement of cell dimensions from powder data by Cohen's method. The average crystallite size of the mixed oxides was estimated according to Debye–Scherrer equation.

The specific surface area was determined by Brunauer–Emmett–Teller (BET) method with a Quantachrome NOVA instrument using Ar as carrier and N_2 as adsorbent.

The X-ray photoelectron spectroscopy (XPS) experiments were carried out on a PHI-Quantera SXM system equipped with a monochromatic Al$K\alpha$ X-rays under UHV (6.7×10^{-8} Pa). A 100 μm spot size was used for analysis. Sample charging during the measurement was compensated by an electron flood gun. The electron takeoff angle was 45° with respect to the sample surface. The XPS data from the regions related to the C 1*s*, O 1*s*, Zr 3*d*, Ce 3*d* and Sr 3*d* core levels were recorded for each sample. The binding energies were calibrated internally by the carbon deposit C 1*s* binding energy (BE) at 284.8 eV.

The high resolution micrographs were shot by a JEOL 2011 high resolution transmission electron microscope (HRTEM), operating at 200 kV. Before the observations, the powder samples were diluted in ethanol and dispersed by ultrasonic. Afterward, a drop of each solution was deposited on a Cu grid coated by a holed carbon film and dried in air. Image analysis was performed on digitized images using Digital Micrograph 3.5.2. Digital diffraction patterns (DDPs) corresponded to the log-scaled power spectrum of the corresponding fast Fourier transformations (FFTs).

In situ diffuse reflectance infrared spectroscopy (DRIFT) studies were performed using an environmental diffuse reflectance IR cell mounted on a Nicolet 6700 FTIR spectrometer (MCT detector). The samples were pretreated in a flow of pure O_2 at 550 °C for 4 h and then purged in pure N_2 for 2 h to clean the surface. For the measurement, 4% CO/N_2 (150 ml/min) was feed to the DRIFT chamber for 15 min, then the gas flow was switched to pure O_2 (12.5 ml/min). Background spectrum of each sample was collected at the very end of pretreatment and subtracted from the reported spectra. The spectra are presented in the form of the Kubelka–Munk function ($F(R)$) which is the equivalent of the absorbance in the diffuse reflectance experiments.

2.3. Oxygen storage/release capacity measurement

Since automotive catalysts suffer rigorous working conditions of high temperature, the OSC properties of the aged samples were extremely concerned. OSC measurement was conducted based on the method proposed by Yao and Yu Yao [23]. The measurements were carried out in a flow reactor system, designed for powder samples and equipped with solenoid valves for rapid introduction of 4% CO/(1% Ar + He) and 2% O_2/(1% Ar + He) pulses. Typically, 25 mg powders were loaded into a 1.0 cm i.d. quartz tube reactor and a total gas flow rate of 300 ml/min was employed. The signals of the outlet gas were detected by an on-line quadrupole mass spectrometer (Omnistar GSD 301 O2).

Two forms of OSC measurements, including successive CO pulse and dynamic CO–O_2 cycle, were applied to measure OSCC and DOSC, respectively. Before the successive CO pulse measurement test, all samples were pre-oxidized in O_2 for 20 min and flushed by He for 30 min at 500 °C. The test procedure consisted of the cycles of 5-s-long CO/(Ar + He) injection and 40-s-long outgassing of pure He on the samples at that temperature. The OSCC was quantified by integrating the concentration of CO_2 produced in the first ten CO/(Ar + He) pulses. In the dynamic CO–O_2 mode, OSC measurement was operated at certain temperatures by alternately injecting CO/(Ar + He) and O_2/(Ar + He) on the samples with duration of 5 s for each gas, which meant a test frequency of 0.1 Hz. DOSC was quantified in terms of micromole of CO_2 per gram of catalyst ($\mu mol_{CO_2}/g_{cat}$) by integrating the concentration of CO_2 produced during every single CO–O_2 cycle. Prior to the OSC measurements, all samples were first heated in O_2 at 300 °C for 20 min.

To further investigate the oxygen release behavior of the samples, a static CO step measurement was conducted at temperatures ranging from 350 to 550 °C. At the beginning of this measurement, a 20-min-long oxidation by O_2 was introduced to the samples. We assumed that the ceria species in the materials entirely existed in the form of Ce^{4+} after this pretreatment. After the oxidation, the samples were purged in pure He for 30 min to remove oxygen from the reactor system and then exposed to the CO/(Ar + He) flow of 300 ml/min for 2 min. The signals of the outlet gas were also collected by the on-line quadrupole mass spectrometer.

3. Results

3.1. Structural and textural properties

The XRD patterns of pure and Sr-containing CZ are shown in Fig. 1a. For fresh samples, the main peaks are consistent with the characteristic peaks of cubic CeO_2, which indicates the formation of homogeneous CeO_2–ZrO_2 solid solutions. In the case of aged samples, the sharpening of the diffraction peaks implies a severe

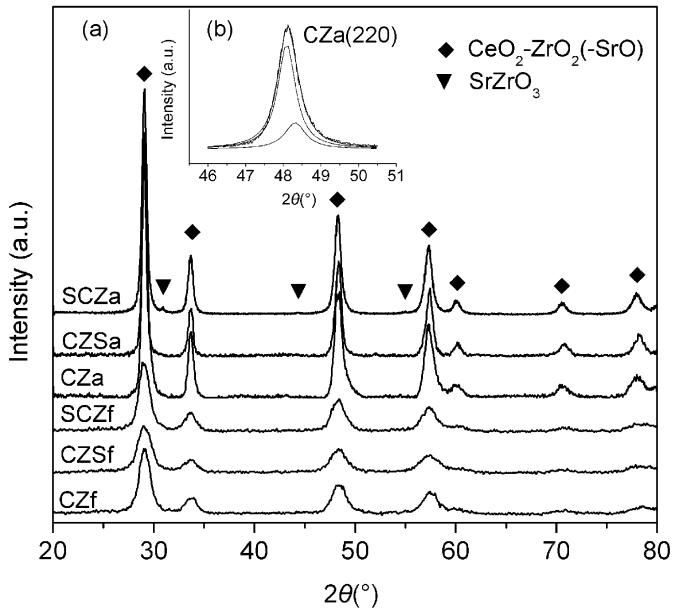

Fig. 1. XRD patterns of all samples (a) and peak fitting of CZa (220) (b).

Table 1
Structural and textural properties of CZ and Sr-containing samples

Samples	S_{BET} (m^2/g)	Crystallite size (nm)	Lattice parameter (Å)	Theoretic lattice parameter (Å)
CZf	56.2	7.2	5.320	5.317
CZSf	63.8	6.9	5.337	5.334
SCZf	56.7	8.1	5.336	5.317
CZa	10.5	43.3	5.336	5.317
CZSa	13.9	30.9	5.327	5.334
SCZa	15.8	17.7	5.338	5.317

sintering of the powders during the calcination at high temperature. Compared with the fresh sample, CZa presents an unsymmetrical peak shape. The numeric fitting of the characteristic peak (220) (Fig. 1b) indicates the segregation of Ce- and Zr-rich phases. On the other hand, no distinct phase separation was observed for SCZa and CZSa, which indicates that Sr^{2+} introduced by either of the employed synthesis methods can stabilize the fluorite-type lattice structure.

For both CZSf and CZSa, no diffraction peaks for Sr-containing compounds are detected, which may be resulted from the following reasons: (1) Sr^{2+} cations have been inserted into the CeO_2–ZrO_2 lattice to form solid solutions, (2) SrO-based clusters are well dispersed on the surface of oxide particles which cannot be detected by XRD. In the case of SCZ samples, however, a small portion of $SrZrO_3$ phase of orthorhombic structure was observed for SCZa. Therefore, it cannot be excluded that, during the ageing treatment, a portion of Zr^{4+} ions have been extracted from the lattice of the mixed oxides and preferentially coordinated with Sr^{2+} to form an orthorhombic phase.

Based on Bragg's law and Debye–Scherrer Equation, the lattice parameters and crystallite sizes of all samples were calculated and the results are listed in Table 1. For comparison, we also applied Vegard's law to calculate the theoretic lattice parameters. According to Kim [24], Vegard's law for ceria-based solid solutions is expressed in the equation:

$$a = 5.411 + \sum(0.0220\Delta r_k + 0.0015\Delta z_k)m_k, \quad (1)$$

where the ionic radius difference is obtained from $\Delta r_k = r_k - r_{Ce}$, the valence difference is derived from $\Delta z_k = z_k - z_{Ce}$, the m_k stands for the molar percentage of the dopant k and 5.411 Å is the lattice constant of cubic CeO_2. The ionic radii (Pauling) taken for calculation are as follows: 0.84 Å for Zr^{4+} and 1.12 Å for Sr^{2+}. For the calculation using Eq. (1), it was assumed that all Ce existed in the form of Ce^{4+} (0.97 Å), while all Sr^{2+} cations were incorporated in CeO_2(–ZrO_2) lattice for CZSf and were dispersed on the surface of CeO_2–ZrO_2 mixed oxides for SCZf. In this way, the theoretic lattice parameter of CZf equals that of SCZf and is smaller than that of CZSf.

The experimental lattice parameters of CZf and CZSf are slightly larger than the theoretic values. This implies the existence of Ce^{3+} (1.14 Å). Compared with CZf, the larger lattice parameter of CZSf confirms the insertion of Sr^{2+} in the oxide lattice. It is interesting that the experimental lattice parameter of SCZf is approximate to that of CZSf rather than CZf. We may attribute this phenomenon to the inward diffusion of surface Sr^{2+} into the bulk of CeO_2–ZrO_2 mixed oxides during the calcination at 700 °C.

In respect that the radius of Zr^{4+} is smaller than that of Ce^{4+} for 8-coordination and a portion of Zr-rich phase has separated out from the mixed oxides, the lattice of CZa expands significantly after the ageing treatment. On the other hand, the lattice of CZSa shrinks as compared with CZSf. Such a lattice shrinkage is partially due to the decrease in concentrations of oxygen vacancies and Ce^{3+} (1.14 Å for 8-coordination) with growing crystallite size [25]. The segregation of Sr from the solid solutions is another important cause; the XPS results in the following discussion will give more details on this point. In the case of SCZa, the size of unit cell remains almost unaltered in comparison with SCZf. This may be resulted from the balance between the extraction of Zr^{4+} from the oxide lattice and the loss of oxygen vacancies and Ce^{3+} along with the growth of crystallites.

Combining the crystallite size with the values of BET surface area reported in Table 1, it can be concluded that the introduction of Sr^{2+} can effectively improve the thermal stability of the textural structure of the mixed oxides. Compared with the doping method, impregnation seems to be more effective for Sr to restrict the growth of oxide crystallites and maintain relatively high surface area.

Specifically, the HRTEM images of CZSa and SCZa were compared to directly publicize the effect of preparation methods by which Sr species were added on the features of the microstructure after ageing treatment. As shown in Figs. 2c and 2d, SCZa does not evidently present an arrangement of atoms in the crystallites as order as CZSa in Figs. 2a and 2b, and part of the grain boundaries are even too blurring to be distinguished. This implies that the crystallinity of CZSa is higher than that of SCZa. It agrees well with the XRD results, declaring that CZSa with larger crystallite size sinters more severely than SCZa.

Moreover, the DDPs of the collected micrographs were applied to assist the phase recognition. According to the diffraction patterns of Figs. 2a, 2b and other images (not shown) taken on CZSa, only one ceria-based mixed oxides phase with cubic fluorite structure is observed. The spots of DDPs in Figs. 2a and 2b were labeled according to the measured spacing values. In the case of SCZa, however, besides the diffraction patterns of ceria-based mixed oxides, additional patterns of an impurity phase (as indicated by white arrows in the insets of Figs. 2c and 2d) were obtained. In Fig. 2c, the selected region exhibits the morphology of two overlapped particles, and the DDPs generally contain two sets of diffraction patterns, belonging to the two particles, respectively. The set with spacing values of 3.0 and 4.8 Å measured for the spots indicated by arrows can be assigned to $(\bar{1}21)$ and $(0\bar{1}1)$ family planes of orthorhombic $SrZrO_3$, and the geometry corresponds to [311] zone axis. Since the bottom particle is assured to be ceria-based mixed oxides according to the inter planar spacing values, the top one is considered to be a $SrZrO_3$ particle. With the zone

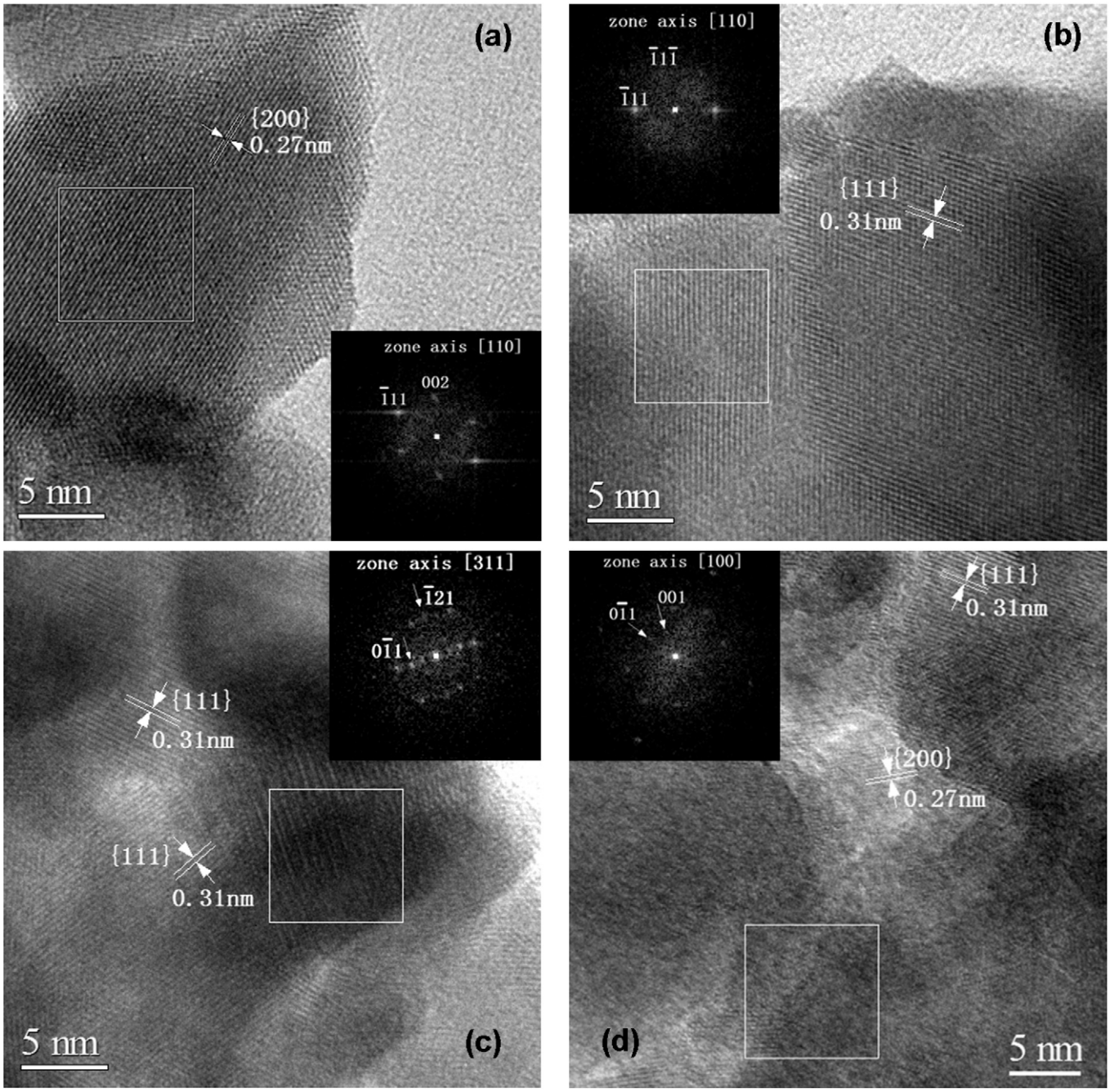

Fig. 2. Representative HRTEM images of (a, b) CZSa and (c, d) SCZa. Insets are the DDPs corresponding to the selected regions in white squares. In (c) and (d), dots indicated by arrows in DDPs possibly reveal the existence of $SrZrO_3$ phase.

axis of [100] in Fig. 2d, the spacing values of the spots indicated by arrows, 5.7 and 4.8 Å, possibly originate from the (001) and $(0\bar{1}1)$ facet families of $SrZrO_3$ phase, respectively. Unfortunately, the morphology of the corresponding region could not be well described because of the imperfect crystallization. As reported in literature [26,27], the common mechanism of the stabilization of surface area with trivalent dopants is a surface dopant enrichment which impedes ceria crystallite growth under oxidizing conditions. In our case, the impregnation method appears to be more efficient to restrain the sintering of oxide particles under rigorous ageing treatment. This phenomenon can be realized because impregnation introduces more Sr species on the surface of oxide particles and consequently disturbs the coalescence of two adjacent ceria-based oxide particles by acting as interlayer. During the ageing treatment, the formation of $SrZrO_3$ crystallites on oxide particles could further baffle the agglomeration and restrain the sintering process.

Hence, combining with the preparation methods used, it can be derived from the XRD and HRTEM observations that (1) high dispersion of Sr^{2+} ions in the bulk of CZSa is not favorable for the $SrZrO_3$ formation, and (2) formation of $SrZrO_3$ crystallites on SCZa are facilitated by the enrichment of surface Sr species on the surface of SCZa, and the $SrZrO_3$ phase distributed on the surface of the oxide particles accounts much for the retardation of the sintering process of ceria-based mixed oxides during the hydrothermal treatment.

Moreover, it is worth noting that the growth of $SrZrO_3$ crystallites is based on the coordination of Sr species with ZrO_2, which segregated out of the ceria-based mixed oxides during the ageing

Table 2
Surface elemental composition and atomic ratio of the samples measured by XPS

Samples	Surface compositions (at%)						Ce/Zr	O/(Ce + Zr + 2Sr)
	Ce		Zr	Sr	O			
	Ce^{3+}	Ce^{4+}			O_{latt}	O_{ads}		
CZf	5.1	15.7	9.3	–	51.9	18.0	2.2	2.3
CZSf	3.7	13.5	8.7	1.7	53.3	19.0	2.0	2.5
SCZf	2.4	9.4	6.4	8.0	31.0	42.8	1.8	2.2
CZa	3.7	10.1	9.5	–	58.5	18.5	1.4	3.3
CZSa	3.7	10.9	8.9	3.2	52.9	20.5	1.6	2.5
SCZa	3.8	10.6	8.9	3.0	51.5	22.3	1.6	2.5

treatment. The difference between the fluorite and orthorhombic lattice structures requires a reorganization of the atoms at the interface of $SrZrO_3/CeO_2$–ZrO_2 mixed oxides, and hereby a lattice distortion at the interface atomic layers could be predictable. The oxygen atoms at the interface are more labile since the effect of structural disorder on the facilitation of oxygen vacancy formation has been well established [3,13]. The further discussion will be given in the part of OSC.

3.2. XPS results

The surface composition and atomic ratios obtained by XPS are listed in Table 2. The surface content of Sr is much higher for SCZf than for CZSf on account of the preparation method. In the case of Sr-doped CZ samples, the content of Sr becomes richer on the surface after ageing treatment, implying a segregation of Sr^{2+} from the CeO_2–ZrO_2 lattice. As more Sr^{2+} cations are distributed on the surface instead of being incorporated in the bulk, an obvious shrinkage of the lattice parameter is detected as mentioned above. For SCZ samples, in respect that the Sr species cover the surface of the oxide particles, the surface contents of Ce and Zr are surely lower for SCZf than those for CZf. It is interesting to find that the surface content of Sr experiences so remarkable a decrease after the ageing treatment that SCZa even shows a lower surface Sr content than CZSa. With the XRD and HRTEM observations taken into account, the unexpectedly low surface content of Sr on SCZa is probably attributed to the following reasons: (1) inward diffusion of Sr into the bulk of CeO_2–ZrO_2 particles and (2) the formation and sintering of $SrZrO_3$ crystallites as detected by XRD. As listed in Table 1, the difference between the lattice parameters of SCZf and SCZa is rather unconspicuous, indicating the portion of inward migrating Sr is quite limited. Therefore, the latter reason would account much for the loss of surface Sr. Since the detection depth of XPS is confined to approximately 15 Å [33], the Sr in the bulk of $SrZrO_3$ particles may be indetectable.

The migration of Zr from the bulk to the surface during ageing process can be indicated by the decrease of Ce/Zr ratios. The gaps between the Ce/Zr ratios of fresh and aged samples are the result of the reorganization of phases with different Zr composition, forming a so-called "shell–core" structure with the high-Zr-composition phase in the outer sphere of the particles. Compared with that of CZ, the Ce/Zr ratios of Sr-containing samples change less, which accords with the XRD results that CZSa and SCZa did not experience any obvious phase segregation. It is noted that there is no difference in Zr at% between CZSa and SCZa though the growth of $SrZrO_3$ requires the extraction of Zr atoms from the ceria-based matrix. Similar as the explanation to the abnormal low surface content of Sr in SCZa, a portion of Zr in the bulk of $SrZrO_3$ may get away from detection of XPS and hereby the surface abundance of Zr is similar to that for CZSa.

Specifically, the oxidation states of Ce and O were analyzed by fitting the curves of Ce 3*d* and O 1*s* spectra obtained from XPS measurements. As shown in Fig. 3, the curves of Ce 3*d* spectra were fitted with eight peaks in accordance with the fitting and

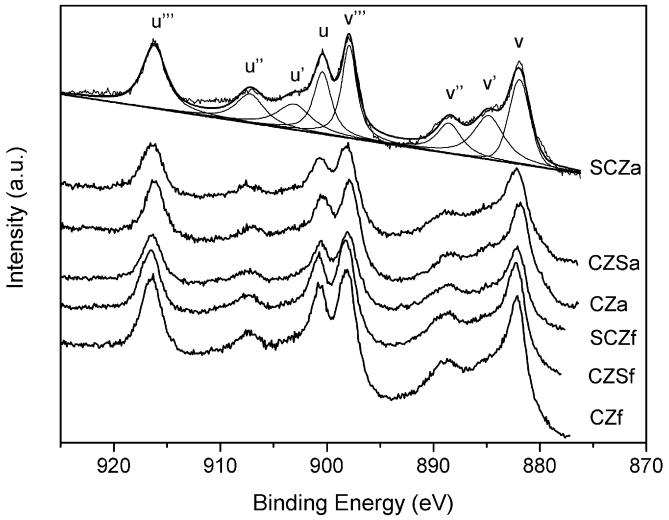

Fig. 3. Ce 3*d* spectra for all samples.

labeling method reported elsewhere [28,29]. The relative percentages of the cerium species were obtained by the area ratios of the Ce^{4+} $3d_{5/2}$ (v, v'' and v''')/Ce^{3+} $3d_{5/2}$ (v'). According to the O/(Ce + Zr + 2Sr) ratios in Table 2, the corresponding values are all higher than 2. This features from the coexistence of chemisorbed oxygen (O_{ads}) with lattice oxygen (O_{latt}). In order to distinguish the two types of oxygen, the spectra for the O 1*s* ionization feature were numerically fitted with two Gaussian–Lorenz features according to earlier reports [30]. The relative percentages of these two oxygen species were quantified based on the area ratios of O_{latt} to O_{ads} peak. It is worth noting that the atomic contents of Ce^{3+}, Ce^{4+} and Zr^{4+} of all aged samples are of great similarity while relatively lower O_{latt} contents were observed on CZSa and SCZa. This observation to some extent indicates the higher abundance of oxygen vacancies, which are created to maintain the charge equilibrium after Sr^{2+} doping [20,22]. Due to the similar Ce^{3+} content, the extra share of oxygen vacancy is deduced to primarily associate with Sr and Zr species instead of Ce, according with the existence of crystal defects at the $SrZrO_3/CeO_2$–ZrO_2 interface.

3.3. OSC properties

The OSC results exhibit high similarity for all fresh samples (not shown), and the OSCC and DOSC values reach as high as ca. 950 and 450 $\mu mol_{CO_2}/g_{cat}$ at 500 °C, respectively. To verify the merit of Sr in promoting the thermal resistance of catalysts, specific attention was paid to the OSC properties of hydrothermally aged samples.

3.3.1. OSCC

The OSC results tested under the successive pulse mode are listed in Table 3. The OSCC values correspond to the reduction ratios (Ce^{3+}/Ce) of 21.7%, 25.8% and 28.9% for CZa, CZSa and SCZa, respectively. This observation highlights the promoted reducibility of Sr-modified CeO_2–ZrO_2 mixed oxides. Dramatically, Sr species introduced by impregnation appear to be more effective than those by doping in promoting the reducibility of the oxides. To make clear whether a portion of active oxygen species originate from $SrZrO_3$, the OSCC of pure $SrZrO_3$ was tested at 500 °C. The result is 64.3 $\mu mol_{CO_2}/g_{cat}$ and is much smaller than the OSCC value of SCZa. In respect that the weight content of Sr in SCZa is only 3%, the low OSCC of $SrZrO_3$ excluded the possibility that the predominance in OSCC of SCZa was due to the contribution of oxygen from $SrZrO_3$.

Table 3
OSCC and amounts of oxygen released during each CO pulse

Samples	Oxygen released in each pulse[a]										OSCC[b]	OSC_{surf}[c]	OSC_{bulk}[d]
	Pulse 1	Pulse 2	Pulse 3	Pulse 4	Pulse 5	Pulse 6	Pulse 7	Pulse 8	Pulse 9	Pulse 10			
CZa	81.7	64.6	56.0	50.2	44.9	40.7	36.1	32.9	30.7	28.8	466.6	39.9	426.7
CZSa	112.1	79.0	62.7	53.7	47.9	42.9	38.8	35.6	32.9	31.0	536.6	52.8	483.8
SCZa	152.5	92.2	68.0	57.1	49.1	44.0	39.3	35.8	33.2	30.5	601.7	60.0	541.7

[a] Given in $\mu mol_{CO_2}/g_{cat}$.
[b] Calculated by summing up the amount of oxygen released in the 10 pulses, given in $\mu mol_{CO_2}/g_{cat}$.
[c] OSC_{surf} ($\mu mol_{CO_2}/g_{cat}$) = $S_{BET} \times 3.8\ \mu mol_{CO_2}/m^2$ [6].
[d] OSC_{bulk} ($\mu mol_{CO_2}/g_{cat}$) = OSCC − OSC_{surf}.

The amount of the most readily releasable oxygen ("fast" OSC) of the oxides was quantified according to the amount of oxygen species that reacted during the first CO pulse, and the results follow the sequence of SCZa > CZSa > CZa. According to the literature [6], a $Ce_{0.68}Zr_{0.32}O_2$ solid solution has a theoretical OSC of 3.8 $\mu mol_O/m^2$ assuming that there is no surface segregation of the Ce^{4+} and Zr^{4+} cations and an equal distribution of the (100), (110), and (111) planes. Meanwhile, it is noted that the theoretical number of surface oxygen atoms (atoms-O/nm^2) differs by no more than 1.5% in the case of $Ce_xZr_{1-x}O_2$ ($x > 0.5$) in either cubic or tetragonal crystal structure. If we take the same value of 3.8 $\mu mol_{CO_2}/m^2$ for our mixed oxides of a similar composition, i.e. atomic ratio of Ce:Zr = 67:33, and take the BET surface areas in Table 1 into consideration, the theoretical OSC supplied by monolayer (OSC_{surf}) of the oxide particles could be figured out as listed in Table 3. Thus, the values of "fast" OSC are ca. 2.0, 2.1 and 2.5 times of the OSC_{surf} on CZa, CZSa and SCZa, respectively. It should be also noted that the calculated OSC_{surf} values are the theoretical upper limitations of surface oxygen atoms since the lattice defects and hereby Ce^{3+} species always exist on the surface of the oxides even after oxidative pretreatment [29,31]. Therefore, it is not arbitrary to deduce that the Ce^{4+} cations not only on the top layer but also in the subsurface were involved in the "fast" OSC. The different multiples also imply that larger surface area was not the only factor to enhance the amount of "fast" OSC, the distribution of Sr in/on the CZ particles acts as another cause in generating labile oxygen. Taking the lower crystallinity into account, we consider the structural disorder on the surface, $SrZrO_3/CeO_2$–ZrO_2 interface for instance, to be relevant to the highest "fast" OSC of SCZa.

From the second to the tenth pulse, oxygen atoms participating in the reaction are considered to be purely released from the bulk of particles. After deducting OSC_{surf} from OSCC, we obtained OSC_{bulk}, which reflects the modification of Sr on the diffusion rate of bulk oxygen in the CZ particles. As proposed above, Sr^{2+} can be incorporated in the lattice of the oxides by both preparation methods. After the hydrothermal ageing, however, a portion of Sr^{2+} extracted from the bulk and migrated to the surface for CZSa while no evident Sr-extraction is observed on SCZa. This may explain the higher OSC_{bulk} of SCZa in comparison with CZSa.

3.3.2. DOSC

The DOSC values of mixed oxides at different temperatures are presented in Fig. 4. The oxidation of CO initiated at ca. 350 °C for all samples and the disparity of DOSC values is more evident at higher temperature. Agreeing well with the OSCC results, DOSC values follow the sequence of SCZa > CZSa > CZa over the whole testing temperature range, confirming the enhanced reducibility of Sr-containing samples.

The concentration curves of produced CO_2 over aged samples are shown in Fig. 5. The same as reported by other research [32,33], two peaks of CO_2 production, located at 1.2–1.8 s and 5.2–5.8 s, respectively, were observed for all samples. According to Descorme et al. [32], the coexistence of CO and gaseous O_2

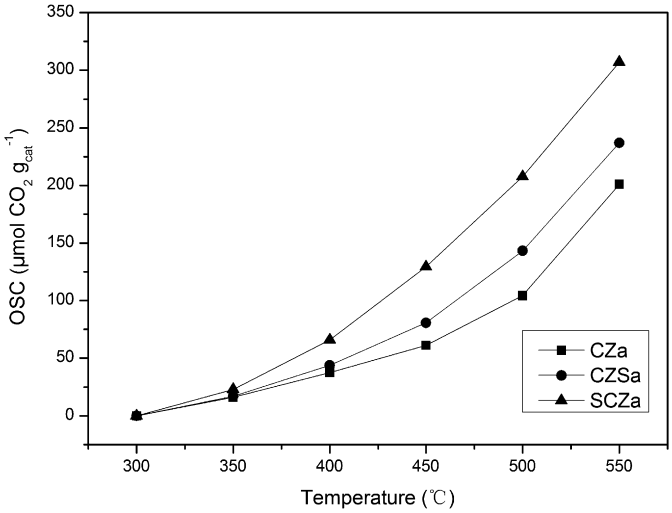

Fig. 4. Dynamic OSC values of aged CZ and Sr-containing samples.

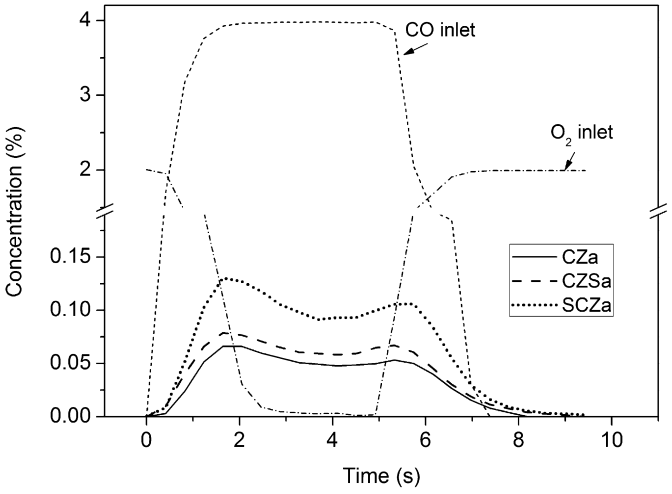

Fig. 5. Concentration curves of gaseous reactants and formed CO_2 for CZa, CZSa and SCZa at 400 °C.

should be taken into the analysis of CO_2 concentration curves. The first peak included CO_2 coming from both the catalytic oxidation of CO in the presence of gaseous oxygen and the oxygen storage reverse reaction. The second CO_2 peak was completely due to the catalytic oxidation of CO since the oxides were partially reduced at this moment. In literature [33], however, two CO_2 peaks were still observed although the catalytic oxidation was avoided by adding He pulses in between CO and O_2 pulses. The authors claimed that the production of CO_2 over ceria passed through the formation of "weakly bonded carbonates" that instantaneously decomposed at 327 °C producing reduced ceria. The first peak was attributed to the immediate desorption of CO_2 after the decompo-

sition of weakly bonded carbonates. The second CO_2 peak observed during the O_2 step could be rationalized considering that more stable carbonates were still present during the O_2 pulse; oxygen then caused the oxidation of the partially reduced ceria and produced the second part of CO_2.

To verify whether catalytic oxidation of CO by gaseous O_2 occurred in this work, the CO step in CO–O_2 cycles and the first pulse in the successive CO pulse measurement were compared. This is based on the fact that the latter purely involves the release of oxygen from oxides and can be regarded to replicate the oxygen storage reverse reaction in the CO–O_2 cycles. Hereby, if the excess of DOSC in comparison with "fast" OSC were detected, the participation of gaseous oxygen in CO oxidation could be testified. Take the case at 500 °C for instance, the DOSC values of CZa, CZSa and SCZa are 23.7, 31.2 and 55.2 $\mu mol_{CO_2}/g_{cat}$ higher than the corresponding "fast" OSC, respectively, meaning that the occurrence of CO oxidation by gaseous oxygen are responsible for the bimodal CO_2 curves.

Meanwhile, *in situ* DRIFTS inspecting the reactions during the CO–O_2 cycles raised more plausible reasons for different shapes of the CO_2 curves. Because of the intrinsic characteristics of FTIR measurement, the CO and O_2 pulses have to be prolonged from 5 s to several minutes. At the time of 1 and 2 min after each gas switching, the mixture of CO and O_2 could be eliminated from the reactor and the reaction would purely deal with the oxygen release/storage of the mixed oxides. The collected spectra in CO and O_2 flow are presented in Figs. 6a and 6b, respectively. For sake of conciseness, attentions are paid to the special wavenumber regimes including CO chemisorption region (2000–2200 cm^{-1}), chemisorbed carbonate region (1200–1800 cm^{-1}), and the region of support skeletal vibrations (800–1000 cm^{-1}). The bands at 2177 and 2125 cm^{-1} accord with the assignment of CO linearly adsorbed on Ce^{4+} and Ce^{3+}, respectively [34]. Although XPS reported that the surface contents of Ce^{4+} and Ce^{3+} on aged samples are similar to each other, the chemisorption capability of these Ce species in CZa and Sr-containing samples are found to behave diversely. Compared with CZa, the absorbance at 2177 and 2125 cm^{-1} are higher for CZSa and SCZa. Primarily, the higher surface area, which allows more Ce species exposed in CO stream, should be taken into account. The two broad bands centered at 1338 and 1567 cm^{-1} are the summation of several overlapping bands located between 1300–1700 cm^{-1}. The main bands here can be attributed to the inorganic carboxylate species or surface carbonate. The absorbance of these two bands evidently increases as the CO stream goes on and drops in the O_2 flow, revealing an affiliation with CO_2 production. The corresponding carbonate species therefore represent the CO_2 bonded in the form of those "more stable carbonate" mentioned above. According to the higher absorbance for Sr-containing samples, it is quite clear that more produced CO_2 will bond onto the materials as carbonates and then desorb during O_2 pulse. This is convincing to explain the longer and more intensified tails (time ranging from 6 to 9 s in Fig. 5) of CO_2 concentration curves for CZSa and SCZa. The presence of other carbonate species is clearly validated by the band at 860 cm^{-1}. The band at 1037 cm^{-1} is assigned to the carbonates bidentate [35], while the CO_2^{2-} carbonite species, which is formed by CO interacting with an oxygen atom near a defect of ceria [36], may be responsible for the band at 1153 cm^{-1}. Owning to the disappearance of these bands on CZa, the carbonate species presented at 860, 1037 and 1153 cm^{-1} are spontaneously tied to Sr-containing carbonate. Regardless of the reductive/oxidative atmosphere, the absorbances for these bands almost keep invariable, and hereby the corresponding carbonates are considered to contribute little to the OSC.

To sum up, CO oxidation by mixed oxides and gaseous oxygen, carbonate formation and decomposition are all responsible for the bimodal profiles of CO_2 in DOSC test. It is worth noting that the

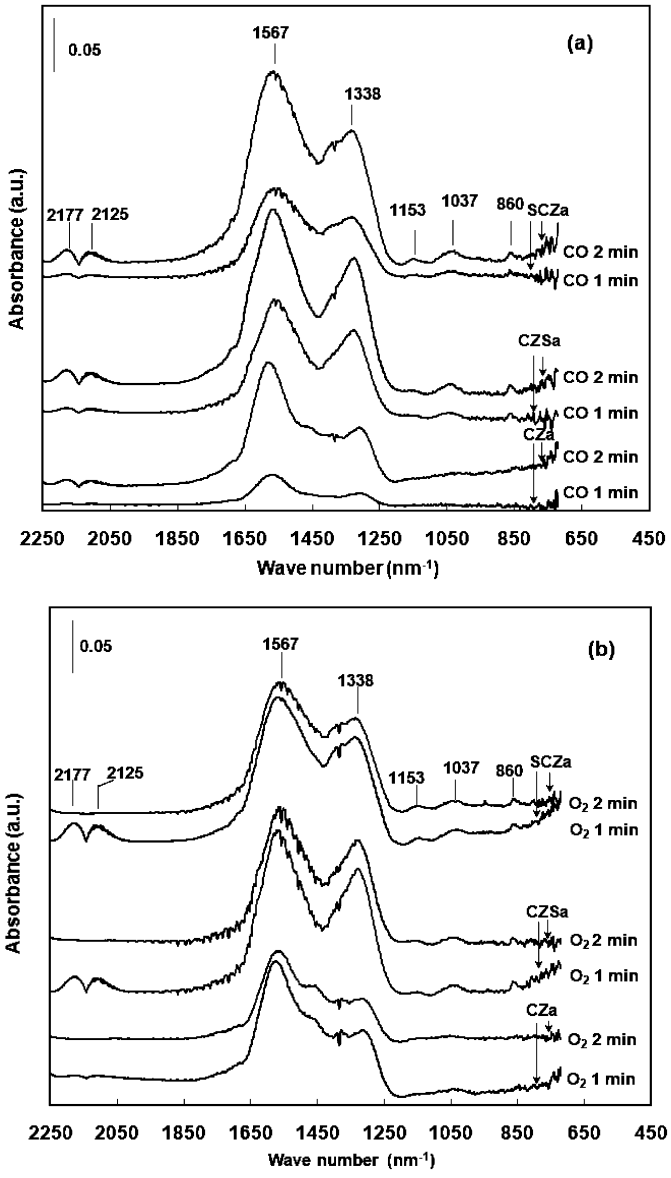

Fig. 6. *In situ* FTIR tests carried on aged CZ and Sr-containing samples: reduction by CO (a) and reoxidation by O_2 (b).

DOSC values at 500 °C are ca. 2.6, 2.7 and 3.4 times larger than the OSC_{surf} for CZa, SCZa and CZSa, respectively. When taking the adsorbed oxygen species and gaseous oxygen in catalytic oxidation into consideration, we would obtain smaller amount of oxygen released from oxides. Therefore, we can deduce that the surface property rather than the bulk property is the determining factor for the dynamic OSC performance, and the particular distribution of Sr on the surface evidently accounts for the superior dynamic OSC of SCZa in our cases.

3.3.3. CO step measurement

Instantaneous CO_2 concentration during the CO step measurement was monitored as a function of time. The instantaneous rates for CO_2 production at certain Ce^{3+}/Ce ratios, denoted as R_{CO_2}, were calculated based on the analyzing method well established by Hori et al. [37]. As shown in Fig. 7, the reduction ratio of the material at the time of interest, t_i, was determined by integrating the CO_2 formed from the start of the pulse, t_0, to t_i. Then, the integrated CO_2 formed was mass balanced with the O atoms that

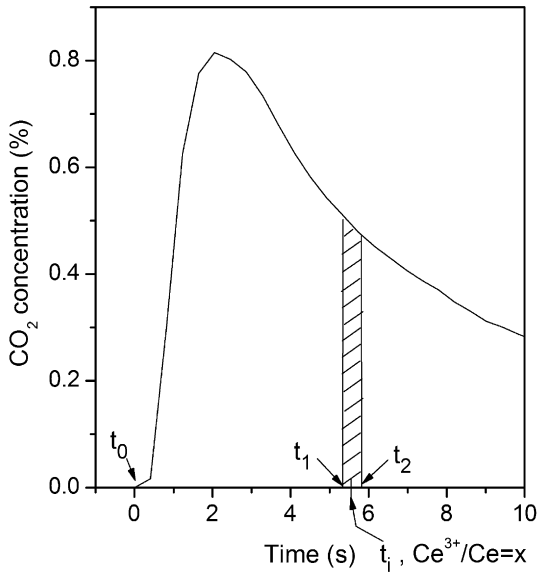

Fig. 7. Schematic representation of the calculation of reaction rates.

left the sample to determine the reduction ratio. R_{CO_2} is defined as follows:

$$R_{CO_2}\left(\mathrm{mol}_{CO_2}/(g_{cat}\,s)\right) = \frac{\int_{t_1}^{t_2} CO_2 \text{ concentration}}{t_2 - t_1}, \quad (2)$$

where the locations of t_1 and t_2 are defined in Fig. 8 and the gap between t_1 and t_2 is generally smaller than 0.1 s.

In Fig. 8, the evolution of R_{CO_2} as a function of temperature (K) is given in Arrhenius coordinates and the activation energy (E_a) for the CO oxidation is estimated according to the slope of the linear function. Arrhenius plots obtained at $Ce^{3+}/Ce = 1.5\%$ (Fig. 8a) and 12% (Fig. 8b) indicate that E_a are to some extent reduction-ratio-dependent. Along with the increase of reduction ratio, the slopes of the linear functions for Sr-containing samples present an intense increase, approaching to that for CZa, while the increment for CZa is relatively low. This suggests that the rate-limiting step for CO oxidation by the oxides changes with the participating oxygen species, which originate from different parts of the particles, and the rate-limiting process for all three materials are the same when the reduction process penetrates into the bulk of the particles.

To carefully examine the point where the rate-limiting step alters, the E_a values were estimated at reduction ratios of 1.5%, 3.0%, 4.5%, 12% and 18%. In view of the theoretical OSC supplied by the top layer of CZSa and SCZa particles, i.e. OSC_{surf} values in Table 3, the reduction ratios of 3.9%, 5.1%, and 5.8% can be roughly regarded as the critical points which separate the status of surface reduction from bulk reduction for CZa, CZSa and SCZa, respectively. These critical points appear quite close to the reduction ratios where the E_a values slow down the climbing pace as shown in Fig. 9. That is to say, the rate-limiting step changes right after the reduction penetrates into the bulk. Specifically, the surface reduction of CZa may share the same rate-determining step with bulk reduction since the variation of E_a is localized in a relatively narrow range. In the case of surface reduction resulting in $Ce^{3+}/Ce = 1.5$, the extremely low E_a for Sr-modified CZ, especially SCZa, symbolizes that a portion of oxygen atoms on the oxide surface are much more labile. Again, the role of surface structure, especially the distribution of Sr on the surface of mixed oxides, is highlighted.

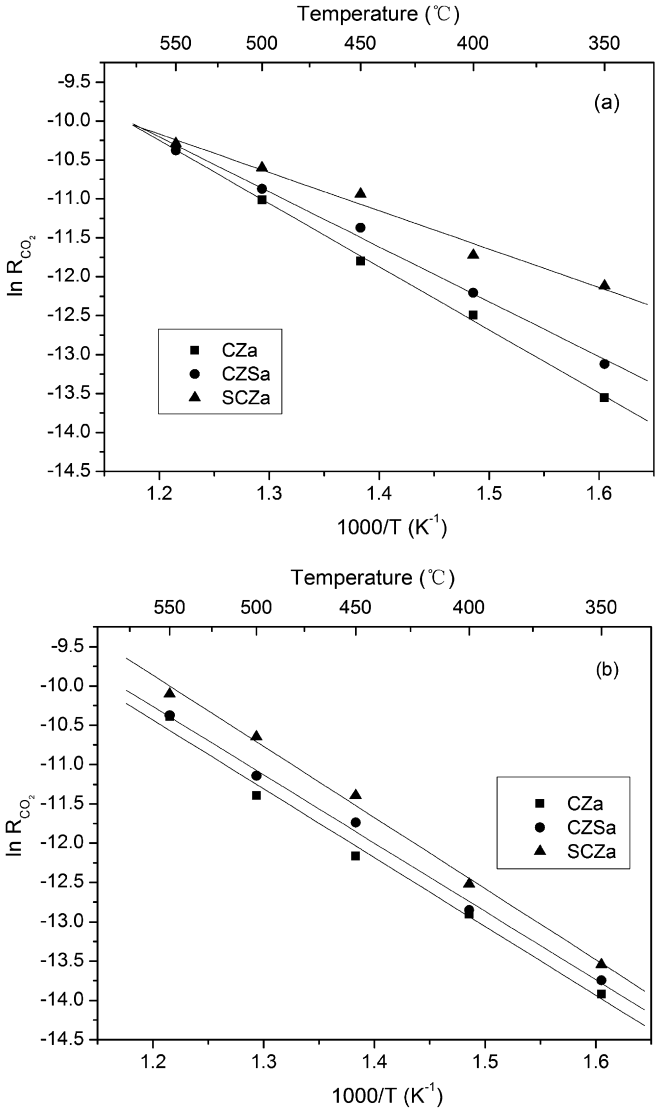

Fig. 8. Arrhenius plots for CZa, CZSa and SCZa when $Ce^{3+}/Ce = 1.5\%$ (a) and 12% (b).

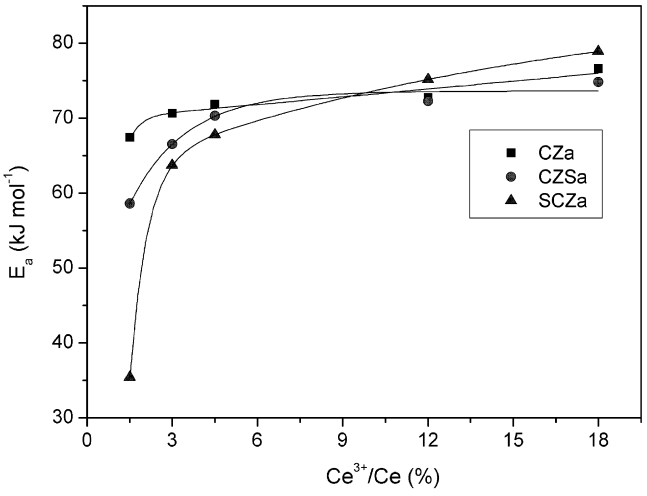

Fig. 9. Activation energies measured at different reduction ratios.

4. Discussion

Based on the theoretical estimation method on OSC per atomic layer and the measured OSC values, it can be summarized that DOSC depends on the amount of activated Ce^{4+} or readily releasable oxygen species on the surface and subsurface of particles, and the penetration depth of reduction increases with temper-

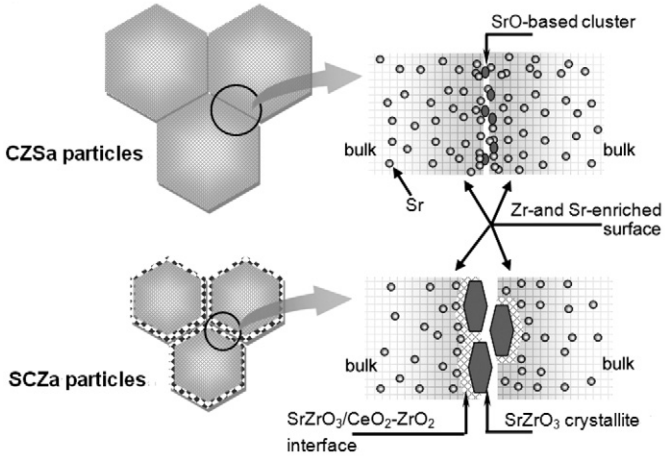

Fig. 10. Schematic of the microstructural features of aged Sr-containing samples.

ature; OSCC and CO step results, however, reflect the reduction procedure deep into the bulk of mixed oxides, and the reduction penetrates deeper along with testing time. For a used (aged) catalyst operating in auto exhaust with A/F perturbations, CO and NO_x begin to break through when the perturbations require more than ~5% of the OSM to store and release oxygen, and a mildly reduced CeO_x ($2 > x > 1.97$, i.e. $6\% > Ce^{3+}/Ce > 0$) material could already match the levels of reduction necessary for good conversion efficiencies over fully formulated catalysts [37]. Thus, regarding the testing conditions, the results of DOSC, "fast" OSC, E_a and R_{CO_2} presented at $Ce^{3+}/Ce < 6\%$, primarily concerning surface reduction, are of special significance. Based on the obtained results, DOSC and "fast" OSC values follow the sequence of SCZa > CZSa > CZa. Focusing on R_{CO_2}, the samples are ranked in the sequence of SCZa > CZSa > CZa through the whole reduction ratio range that draws interests, and correspondingly, the E_a values for the surface reduction of CZa, CZSa and SCZa are arrayed as SCZa > CZSa > CZa. All these results confirm the effect of Sr on promoting the reducibility of Ce^{4+} or readily releasable oxygen species on the oxide surface. Accordingly, the features of surface structure become crucial for the oxygen release performance of the hydrothermally aged oxide particles.

The microstructural characteristics of the aged Sr-containing samples are schematically summarized in Fig. 10. As revealed by XRD, XPS and HRTEM observations, Sr^{2+} can be incorporated into the lattice of CZ by both doping and impregnation methods, and hereby favors the formation of oxygen vacancies by compensating the excess negative charge and generating lattice distortion [38]. After the hydrothermal ageing, CZSa and SCZa present similar surface composition, and Sr^{2+} and Zr^{4+} are enriched in the surface and subsurface atomic layers of the particles. The difference is that the XRD and HRTEM techniques could hardly detect the existence of individual SrO-based phase on CZSa while confirming the formation of $SrZrO_3$ phase on SCZa. It is deduced that Sr^{2+} on the surface of CZSa is probably ionically enriched in the lattice or exists in fine amorphous clusters. Nano-sized $SrZrO_3$ particles on SCZa are observed on oxide particles. In view of the preparation method, the highly enriched Sr on SCZ surface can disturb the coalescence of two adjacent matrix particles, which simultaneous restricts the crystallization, growth and sintering of oxide particles. Meanwhile, the surface Sr-enrichment facilitates the formation of $SrZrO_3$ particles, which can further baffle the agglomeration and restrain the sintering of CZ particles. It is worth noting that the formation and growth of these $SrZrO_3$ particles results from a competition between Sr species and Ce species for the coordination with ZrO_2. Since the lattice structures of $SrZrO_3$ and CeO_2–ZrO_2 mixed oxides are quite different, the atomic reorganization at the interface of $SrZrO_3/CeO_2$–ZrO_2 is deserved to occur. The existence of readily releasable oxygen at oxides/oxides interface has been reported by [39] and references therein. In our case, the oxygen ions located at the interface of $SrZrO_3/CeO_2$–ZrO_2 are tentatively assigned as the species presenting higher activity. Sr species ionically dispersed in the lattice of CeO_2, as in the case of CZSa, may be functional at a discount.

5. Conclusions

The introduction of Sr to CeO_2–ZrO_2 mixed oxides by doping (CZS) or impregnation method (SCZ) is effective in retarding the sintering of oxide particles and maintaining high surface area after hydrothermal ageing. Meanwhile, the ageing-treatment-induced segregation of phases with different Zr contents can be restricted by the incorporation of Sr^{2+} via both methods. Specifically, the impregnated Sr species, with a portion of surface Sr coordinating with ZrO_2 to form $SrZrO_3$ phase during the ageing process, exhibit more evident effect in decelerating the crystallization and sintering of oxide particles. Dynamic OSC and OSCC results expose the promoted reducibility held by the Sr-containing samples, especially for SCZa, due to the predominance of labile oxygen from surface and subsurface layers. The CO step measurement shows that the E_a value for CO oxidation over the oxides depends on the reduction ratio. At low reduction ratio, theoretically dealing with surface reduction, the E_a for Sr-containing samples, especially SCZa, can be much lower than that for CZa. This indicates the existence of a certain kind of active oxygen species on the particle surface. The specific surface structure features concerning Sr distribution are considered to be primarily responsible for the creation of highly active oxygen. Taken the formation of $SrZrO_3$ particles and the atomic reorganization at the oxides/oxides interface into account, oxygen ions located at the $SrZrO_3/CeO_2$–ZrO_2 interface are tentatively considered to be of higher activity and are consequently responsible for the promoted OSC properties.

Acknowledgments

The authors would like to acknowledge the Ministry of Science and Technology, PR China for the financial support of Project 2004CB719503, 2006AA060305 and National Natural Science Foundation of China for the financial support of Project 50502023. Moreover, we would also thank the Center of Analysis and Key Lab of Advanced Materials in Tsinghua University.

References

[1] N. Hickey, P. Fornasiero, J. Kašpar, J.M. Gatica, S. Bernal, J. Catal. 200 (2001) 181.
[2] H.S. Gandhi, G.W. Graham, R.W. McCabe, J. Catal. 216 (2003) 433.
[3] J. Kašpar, P. Fornasiero, M. Graziani, Catal. Today 50 (1995) 285.
[4] R. Di Monte, J. Kašpar, Catal. Today 100 (2005) 27.
[5] M. Boaro, M. Vicario, C. de Leitenburg, G. Dolcetti, A. Trovarelli, Catal. Today 77 (2003) 407.
[6] Y. Madier, C. Descorme, A.M. Le Govic, D. Duprez, J. Phys. Chem. B 103 (1999) 10999.
[7] Z.C. Kang, L. Eyring, J. Solid State Chem. 155 (2000) 129.
[8] S. Bernal, G. Blanco, M.A. Cauqui, A. Martín, J.M. Pintado, A. Galtayries, R. Sporken, Surf. Interface Anal. 30 (2000) 85.
[9] J.P. Cuif, G. Blanchard, O. Touret, A. Seigneurin, M. Marczi, E. Quéméré, SAE Paper 970463, 1997.
[10] M. Boaro, C. de Leitenburg, G. Dolcetti, A. Trovarelli, J. Catal. 193 (2002) 338.
[11] T. Masui, K. Koyabu, K. Minami, T. Egawa, N. Imanaka, J. Phys. Chem. C 111 (2007) 13892.
[12] M. Yashima, H. Takashina, M. Kakihana, M. Yoshimura, J. Am. Ceram. Soc. 77 (1994) 1869.
[13] E. Mamontov, T. Egami, R. Brezny, M. Koranne, S. Tyagi, J. Phys. Chem. B 104 (2000) 11110.
[14] K. Minami, T. Masui, N. Imanaka, L. Daib, B. Pacaud, J. Alloys Compd. 408–412 (2006) 1132.

[15] Y. Nagai, T. Yamamoto, T. Tanaka, S. Yoshida, T. Nonaka, T. Okamoto, A. Suda, M. Sugiura, Catal. Today 74 (2002) 225.
[16] F. Dong, A. Suda, T. Tanabe, Y. Nagai, H. Sobukawa, H. Shinjoh, M. Sugiura, C. Descorme, D. Duprez, Catal. Today 93–95 (2005) 827.
[17] M. Sugiura, Catal. Surv. Asia 7 (2003) 77.
[18] H. He, H.X. Dai, K.W. Wong, C.T. Au, Appl. Catal. A Gen. 251 (2003) 61.
[19] X. Wu, X. Wu, Q. Liang, J. Fan, D. Weng, Z. Xie, S. Wei, Solid State Sci. 9 (2007) 636.
[20] M. Fernández-García, A. Martínez-Arias, A. Guerrero-Ruiz, J.C. Conesa, J. Soria, J. Catal. 211 (2002) 326.
[21] H. Inaba, H. Tagawa, Solid State Ionics 83 (1996) 1.
[22] Y. An, M. Shen, J. Wang, J. Alloys Compd. 441 (2006) 305.
[23] H.C. Yao, Y.F. Yu Yao, J. Catal. 86 (1984) 254.
[24] D.J. Kim, J. Am. Chem. Soc. 72 (1989) 1415.
[25] F. Zhang, S.-W. Chan, J.E. Spanier, E. Apak, Q. Jin, R.D. Robinson, I.P. Herman, Appl. Phys. Lett. 80 (2002) 127.
[26] J.E. Kubsch, J.S. Rieck, N.D. Spencer, in: A. Crucg (Ed.), Catalysis and Automotive Pollution Control, vol. II, Elsevier, Amsterdam, 1991, pp. 125–138.
[27] P.G. Harrison, D.A. Creaser, B.A. Wolfindale, K.C. Waugh, M.A. Morris, W.C. Mackrodt, in: T.J. Dines, C.H. Rochester, J. Thomson (Eds.), Catalysis and Surface Characterisation, The Royal Society of Chemistry, Cambridge, 1996, pp. 76–86.
[28] F.B. Noronha, E.C. Fendley, R.R. Soares, W.E. Alcarez, D.E. Resasco, Chem. Eng. J. 82 (2001) 25.
[29] J. Fan, X. Wu, X. Wu, Q. Liang, R. Ran, D. Weng, Appl. Catal. B Environ. 81 (2008) 38.
[30] S. Ricote, G. Jacobs, M. Milling, Y. Ji, P.M. Patterson, B.H. Davis, Appl. Catal. A Gen. 303 (2006) 35.
[31] J. Fan, X. Wu, L. Yang, D. Weng, Catal. Today 126 (2007) 303.
[32] C. Descorme, R. Taha, N. Mouaddib-Moral, D. Duprez, Appl. Catal. A Gen. 223 (2002) 287.
[33] M. Boaro, F. Giordano, S. Recchia, V.D. Santo, M. Giona, A. Trovarelli, Appl. Catal. B Environ. 52 (2004) 225.
[34] A. Holmgren, B. Andersson, D. Duprez, Appl. Catal. B Environ. 22 (1999) 215.
[35] A. Holmgren, F. Azarnoush, E. Fridell, Appl. Catal. B Environ. 22 (1999) 49.
[36] E. Guglielminotti, F. Boccuui, J. Mol. Catal. A Chem. 104 (1996) 273.
[37] C.E. Hori, A. Brennera, K.Y.S. Ng, K.M. Rahmoeller, D. Belton, Catal. Today 50 (1999) 299.
[38] A. Trovarelli, Catalysis by Ceria and Related Materials, vol. 2, Imperial College Press, London, 2001, p. 73.
[39] E. Mamontov, R. Brezny, M. Koranne, T. Egami, J. Phys. Chem. B 107 (2003) 13007.